Phyton-
International Journal of
Experimental Botany

Tech Science Press

http://doi.org/10.32604/phyton.2026.080926

ARTICLE

In Silico Prioritization of Plant Growth Regulators as Candidate Modulators of Microalgal Lipid Biosynthesis for Biofuel Production

Hanane Oucif[1,2,*], Miloud Benaissa[1,2], Leila Saddikioui[3], Nadia Y. Asfouri[3], Meriem F. Meliani[1], Zineb Belhamra[1,2] and Djilali Baghdadi[1,2]

[1]Department of Biological Sciences, Faculty of Natural and Life Sciences, Ahmed Zabana University of Relizane, Relizane, Algeria
[2]Laboratory of Environment and Sustainable Development, Ahmed Zabana University of Relizane, Relizane, Algeria
[3]Higher School of Biological Sciences of Oran, BP 1042 Saim Mohamed, Cité Emir Abdelkader, Oran, Algeria
*Corresponding Author: Hanane Oucif. Email: hanane.oucif@univ-relizane.dz

Received: 18 February 2026; Accepted: 18 May 2026; Published: 29 June 2026

ABSTRACT: Enhancing lipid productivity in microalgae is a critical goal for advancing sustainable biofuel production. Among emerging strategies, the supplementation of plant growth regulators (PGRs) has gained attention as a potential approach for modulating microalgal metabolism. This *in silico* study evaluated the predicted binding of sixty-five PGRs from 11 chemical classes to five microalgal enzymes associated with lipid biosynthesis, (FabD, KASII, FabG, FATA, and GPAT) using an integrative computational workflow combining virtual screening, molecular docking, molecular dynamics (MD) simulations, and density functional theory (DFT) calculations. Structure-based screening identified fifty-eight compounds with docking scores below −5.0 kcal/mol, consistent with candidate interactions at catalytically relevant regions. Strigolactones and cytokinins emerged as particularly promising families, with several members showing comparatively strong predicted binding affinities. Five phytohormones (STGA, STG, OROB, ZOG, and DHZMP) were prioritized for detailed analysis. MD simulations over 100 ns supported the persistence of predicted protein-ligand complexes, while DFT descriptors provided complementary electronic characterization of these ligands. Together, these computational results highlight a subset of PGRs as candidate binders of key enzymes in fatty acid and TAG biosynthesis pathways. These hypothesis-generating findings require experimental validation to assess their biological relevance and potential contribution to strategies aimed at improving microalgal lipid productivity for biofuel applications.

KEYWORDS: Lipid; microalgae; plant growth regulator; candidate binders; computational

1 Introduction

Microalgae, comprising prokaryotic cyanobacteria and eukaryotic photosynthetic protists, are the most abundant primary producers and play a fundamental role in aquatic food webs [1]. They contribute to nearly half of global oxygen production and primary productivity. Owing to their robust photosynthetic ability, rapid growth, and efficient nutrient conversion, microalgae are increasingly valued across diverse industries [2]. The increasing demand for sustainable energy has intensified interest in alternative biofuels, with microalgae recognized as promising candidates [3]. These organisms can convert atmospheric carbon dioxide into lipid-rich biomass suitable for biodiesel and other biofuels. Biodiesel production relies on polyunsaturated fatty acids (PUFAs) and triacylglycerols (TAGs) accumulated in microalgal cells, yet maximizing lipid yields remains technically challenging [4]. Strategies such as genetic engineering, culture

optimization, and nutrient stress induction have been explored [5], but often face limitations including higher costs, impaired growth, or unstable yields [6].

Phytohormones (PH) and different plant growth regulators (PGRs), such as auxins, cytokinins, gibberellins, abscisic acid, ethylene, salicylic acid, polyamines, betaines, jasmonates, brassinosteroids, and strigolactones, have been extensively studied in higher plants for their roles in enhancing plant yields and stress responses [7]. Recent reports suggest that exogenous application of these compounds can also enhance microalgal biomass accumulation and influence metabolic pathways, promoting metabolite biosynthesis while maintaining cell viability [8]. Such treatments may affect enzymatic activities in lipid metabolism, increase photosynthetic efficiency, or trigger adaptive stress responses that favor lipid storage [2]. Physiological studies have documented increased lipid productivity in microalgae treated with, auxins (IAA, IBA), cytokinins (K, cZ, 6-BAP), gibberellins (GA3), strigolactones, abscisic acid, methyl jasmonate, brassinolide (BL), epi-BL, and salicylic acid [9].

Despite these observations, many PGRs remain underexplored, with more than 70 brassinosteroids [10] and over 250 gibberellins described. Auxins include several indole derivatives, and cytokinins encompass multiple adenine analogues. A cost-effective and rapid screening strategy is therefore needed to prioritize compounds for *in vivo* assays [11]. Computational modeling offers a complementary approach, enabling the prediction of candidate binding interactions and electronic properties without the resource demands of experimental trials. Such insights may guide the rational selection of PGRs for further study in lipid biosynthesis and accumulation.

This study represents an *in silico* exploration of sixty-five PGRs as candidate binders of microalgal lipid biosynthesis enzymes. Five representative proteins were selected–FabD, KASII, FabG, FATA, and GPAT–covering initiation, elongation, reduction, termination, and assembly steps of fatty acid and triacylglycerol pathways. An integrative computational workflow was applied, combining virtual screening, molecular docking, molecular dynamics (MD) simulations, and density functional theory (DFT) calculations. The pipeline is designed to generate hypotheses by identifying predicted binding modes, candidate interactions at catalytically relevant regions, and supplementary electronic descriptors. These computational findings are intended to prioritize ligands for subsequent enzymatic and cellular validation, with the broader aim of informing strategies to enhance microalgal lipid productivity for biofuel applications.

2 Methods

2.1 Preparation of Ligands

Ligand structures were retrieved from the PubChem database [12]. A total of sixty-five plant growth regulators representing eleven chemical classes (Table 1) were selected to ensure structural diversity. Each compound was initially pre-optimized using the MMFF94 force field. Conformational searches were performed, and the lowest-energy conformer was retained. Final geometry optimization was performed at the same level of theory as implemented in AVOGADRO software [13]. The optimized structures were subsequently used as input ligands for molecular docking simulations against the selected microalgal enzymes.

Table 1: List of ligand compounds investigated.

Classes	Ligand Name	Abbreviations	PubChem CID
Abscisic acid	Abscisic acid	ABA	5280896
Salicylic acid	Salicylic acid	SA	338
Strigolactones	(+)-5-deoxystrigol	5-DS	15102684
	(+)-Orobanchol	OROB	10665247
	(+)-Orobanchyl acetate	OROBA	24796587
	(+)-Strigol	STG	5281396
	(+)-Strigylacetate	STGA	15102669
	Sorgolactone	SGL	5281395
	epi-(+)-Strigolactone GR24	GR24	3036799
Jasmonates	Jasmonic acid	JA	5281166
	12-oxo-phytodienoic acid	OPDA	5280411
	Dinor-12-oxo phytodienoic acid	DN-OPDA	644074
	Methyljasmonate	MEJA	5281929
Gibberellins	Gibberellin A1	GA1	5280379
	Gibberellin A3	GA3	6466
	Gibberellin A4	GA4	92109
	Gibberellin A5	GA5	443464
	Gibberellin A6	GA6	443449
	Gibberellin A7	GA7	92782
Brassinosteroids	Brassinolide	BL	115196
	24-Epibrassinolide	EPBL	443055
	28-Homo-brassinolide	HOBL	102601290
	Castasterone	CS	133534
	24-Epicastasterone	EPCS	11812633
	28-Homo-castasterone	HOCS	5487654
Auxins	2-oxindole-3-acetic acid	OXIAA	3080590
	2-phenylacetic acid	PAA	999
	4-chloroindole-3-acetic acid	4-CL-IAA	100413
	Indole-3-acetaldoxime	IAOX	439854
	Indole-3-acetamide	IAM	397
	Indole-3-acetic acid	IAA	802
	3-indoleacetonitrile	IAN	351795
	Indole-3-butyric acid	IBA	8617
	Indole-3-carboxylic acid	ICA	69867
	3-indolepropionic acid	IPA	3744
	Indole-3-pyruvic acid	IPA	803
Cytokinins	6-benzylaminopurine	6-BAP	62389
	Cis-zeatin	CZ	688597
	Cis-zeatin riboside	CZR	13935024
	Cis-zeatin riboside monophosphate	CZRMP	23724752
	Cis-zeatin-9-glucoside	CZ9G	101921807
	Cis-zeatin-O-glucoside	ZOG	5280589
	Dihydrozeatin	DHZ	32021
	Dihydrozeatin riboside	DHZR	10522005
	Dihydrozeatin riboside-5′-monophosphate	DHZMP	72989203
	Dihydrozeatin 9-N-glucoside	DHZ9G	25201996
	Dihydrozeatin-O-glucoside	DHZOG	23724755
	Kinetin	K	3830
	N6-(D2-isopentenyl) adenine	IP	92180
	N6-(D2-isopentenyl) adenosine	IPR	24405
	N6-(D2-isopentenyl) adenosine-5′-monophosphate	IPRMP	10180201
	N6-(D2-Isopentenyl) adenine-9-glucoside	IP9G	25200472
	Trans-zeatin	TZ	449093
	Trans-zeatin riboside	TZR	6440982
	Trans-zeatin riboside 5′-monophosphate	TZRMP	11561034
	Trans-zeatin-O-glucoside riboside	TZROG	169447788
	Trans-zeatin-9-glucoside	TZ9G	9842892
	Trans-zeatin-O-glucoside	TZOG	5461146

Table 1: *Cont.*

Classes	Ligand Name	Abbreviations	PubChem CID
Polyamines	Spermine	SP	1103
	Spermidine	SPD	1102
	Putrescine	PUT	1045
Betaines	Glycine betaine	GB	247
	Delta-aminovaleric acid betaine	AVB	14274897
	Gamma-butyrobetaine	ABB	725
Ethylene	Ethephon	ETH	27982

2.2 Preparation of Target Enzymes

Five enzymes were selected from the Protein Data Bank (PDB) to represent key steps in fatty acid synthesis (FAS) and glycerolipid assembly pathways. The crystal structures retrieved from the RCSB database included: malonyl-CoA:ACP transacylase (FabD; PDB: 4RR5) [14], β-ketoacyl-ACP synthase II (KASII; PDB: 1E5M) [15], 3-oxoacyl-ACP reductase (FabG; PDB: 4DMM) [16], acyl-ACP thioesterase (FATA; PDB: 9MQF) [17], and glycerol-3-phosphate acyltransferase (GPAT; PDB: 8IA1) [18]. These enzymes cover initiation, elongation, reduction, termination, and assembly steps, providing a comprehensive view of the plastidial Type II FAS system found in green algae (*Chlamydomonas reinhardtii*, *Myrmecia incisa*) and cyanobacteria (*Synechocystis*, *Synechococcus*). Structural parameters and biological origins are summarized in Table S1 (Supplementary Data). Protein structures were prepared using BIOVIA Discovery Studio Visualizer 2024 [19] by removing heteroatoms, co-crystallized ligands, and solvents to optimize docking conditions. Hydrogen atoms were added, and the charges were adjusted. Final corrections were performed using Swiss-PdbViewer [20].

2.3 Virtual Screening and Molecular Docking

Virtual screening based on molecular docking was performed to prioritize candidate ligands among the sixty-five plant growth regulators. Docking was carried out against the active site of the five target proteins involved in lipid metabolism using AutoDock Vina, as implemented in the PyRx software platform [21]. The search center (SC) coordinates and box dimensions (BD) applied in docking are provided in Table S2 (Supplementary Data). To validate the docking protocol and establish benchmarks for binding affinities, reference ligands were included alongside the screened compounds. These reference molecules comprised natural substrates (malonyl-CoA for FabD, NADPH for FabG, and sn-glycerol-3-phosphate for GPAT), substrate analogues (PN7 hexanoyl-mimetic for KASII and oleic acid for FATA), and known inhibitors (corytuberine for FabD, platensimycin for KASII, luteolin for FabG, WP2 spirolactam for FATA, and FSG67 for GPAT). All reference ligands were retrieved from their corresponding PDB entries or PubChem and prepared using the same protocol as the plant growth regulators. From the docking outputs, compounds with the most favorable binding energy scores were selected within each ligand class, and the five strongest candidate interactions with microalgal proteins were identified. Predicted binding modes and interaction profiles were visualized and analyzed using BIOVIA Discovery Studio Visualizer [19].

2.4 Molecular Dynamics

Molecular dynamics (MD) simulations were performed using GROMACS 2024.1 [22] to evaluate the structural integrity and dynamic behavior of the protein–ligand complexes identified in docking (STGA/FabD, KASII/ZOG, FabG/STG, FATA/OROB, DHZMP/GPAT). For system preparation, hydrogen atoms were added to the protein structures, which were then solvated in a cubic water box with a 1.2 Å

margin using the TIP3P water model. Na^+ and Cl^- ions were introduced to neutralize the overall charge. The AMBER99SB-ILDN force field was applied to proteins, while ligands were parameterized using the Generalized Amber Force Field 2 (GAFF2). Energy minimization was performed in two steps: 5000 iterations of the steepest descent algorithm followed by 5000 iterations of the conjugate gradient method, with a uniform 10 Å cutoff for van der Waals interactions. The equilibration phase consisted of a 1 ns run under constant volume and temperature (NVT) conditions at 298.15 K. Production simulations were then carried out for 100 ns under constant pressure and temperature (NPT) conditions, employing a 2 fs time step and periodic boundary conditions. Post-simulation trajectory analyses included root mean square deviation (RMSD), root mean square fluctuation (RMSF), hydrogen bonds profiles, radius of gyration (Rg), and solvent-accessible surface area (SASA). MATLAB [23] was used for visualization of the results.

2.5 Density Functional Theory (DFT)

Density functional theory (DFT) calculations were performed for the prioritized ligands using Gaussian 09 [24]. The geometries were optimized using the B3LYP functional and 6-311G (d, p) basis set [25]. Results were analysed with GaussView 5.0 [26]. Electronic descriptors were derived, including frontier molecular orbitals (FMO), molecular electrostatic potential (MEP), and global chemical reactivity parameters. These included total energy, dipole moment, HOMO and LUMO energies, energy gap (ΔE), absolute hardness (η), global softness (σ), chemical potential (μ), electronegativity (χ), ionization energy (IE), electron affinity (EA), and electrophilicity index (ω) [27]. The minimum-energy conformer obtained from docking (PDB format) was used as the input structure for the DFT calculations. These descriptors provide supplementary electronic characterization of the ligands under gas-phase conditions and are intended to highlight candidate charge-transfer properties and kinetic stability.

3 Results and Discussion

3.1 Overview from Virtual Screening

Structure-based virtual screening was performed to prioritize candidate binders of microalgal enzymes involved in lipid metabolism. For each compound, the best docking mode was retained. Fifty-eight molecules showed predicted binding energies below −5.0 kcal/mol, consistent with candidate interactions at the active sites of the five target enzymes. These compounds span eight phytohormone families: strigolactones, cytokinins, brassinosteroids, gibberellins, auxins, jasmonates, abscisic acid, and salicylic acid. In contrast, betaines, polyamines, and ethephon exhibited weaker predicted affinities (above −5.0 kcal/mol) and are considered less promising (Table S3, Supplementary Data). This observation aligns with previous reports indicating that ethephon treatment did not alter lipid content or gene expression in microalgal biomass [28].

Twenty-two molecules were prioritized across phytohormone classes, including strigolactones (OROB, STG, 5-DS, STGA), cytokinins (TZROG, ZOG, TZ9G, DHZMP), brassinosteroids (CS, EPCS, BL, and EPBL), gibberellins (GA7, GA3, GA6, GA4), auxins (IBA, IPA2, PAA, OXIAA), as well as ABA and SA. These compounds represent the chemical diversity of phytohormones with predicted candidate interactions at microalgal lipid metabolism enzymes. This observation is consistent with physiological studies reporting that exogenous 24-epibrassinolide was associated with lipid accumulation, a higher proportion of C16:C18 fatty acids, and upregulation of lipid-related genes such as ACP thioesterase (FATA) in *Botryococcus braunii* B12 [29], biotin carboxylase (BC), and fatty acid desaturase (FAD) in *Chlorella pyrenoidosa* ZF [28], and ω-3 fatty acid desaturase (FAD) in *Chlorella vulgaris* strains [30]. Previous studies have reported that GA3 treatment in *Botryococcus braunii* B12 was associated with increased lipid accumulation and upregulation of genes related to fatty acid biosynthesis, including ACP, BC, FAD, KAS, and MCTK [29]. In *Scenedesmus*

obliquus, treatments with BAP and GA under nitrogen limitation were reported to be associated with increased lipid accumulation and upregulation of genes involved in fatty acid and TAG biosynthesis, including ACP, SAD, FATA, and DGAT [31]. Furthermore, treatments with IAA and ABA in microalgal cells were reported to be associated with ~20–21% increases in lipid content, together with upregulation of fatty acid biosynthesis genes such as ACP, MCTK, and FATA [32]. Similarly, salicylic acid application in *Phaeodactylum tricornutum* was associated with an ~88% increase in lipid content [33].

3.2 Ligand Receptor Affinity

According to the docking results, STGA, ZOG, STG, OROB, and DHZMP emerged as the top-scoring ligands, with predicted binding energies ranging from −8.3 to −11.3 kcal/mol. These strigolactone and cytokinin derivatives exhibited stronger predicted affinities than several reference inhibitors and substrate analogues, consistent with candidate interactions at catalytically relevant regions of FabD, KASII, FabG, FATA, and GPAT (Table 2). The binding poses suggest possible competition with reference ligands, pending experimental validation. As these enzymes mediate key steps in fatty acid and triacylglycerol (TAG) biosynthesis, the prioritized ligands represent hypothesis-generating candidates for further study. This observation is consistent with previous reports in which strigolactones and cytokinins were associated with enhanced lipid accumulation and upregulation of genes involved in carbon fixation and lipid synthesis, including rbcL, accD, KAS III, DGAT, PEPC, ME [31,34,35], as well as ACP, SAD, FATA, FAD, MCTK, and DGAT [28–31]. These parallels support the prioritization of the identified compounds while underscoring the need for experimental validation to determine their biological relevance.

Table 2: Best ligand-receptor affinity.

Target	Ligands	Binding Energies (kcal/mol)	Classes
FabD	STGA	−8.3	Strigolactones
	GR24	−8.2	
	SGL	−7.9	
	STG	−7.8	
	OROBA	−7.8	
	Malonyl-CoA	−7.4	Natural substrate
	Corytuberine	−8.2	Standard inhibitor
KASII	ZOG	−8.7	Cytokinins
	TZOG	−8.5	
	6-BAP	−8.0	
	SGL	−7.9	Strigolactones
	STGA	−7.8	
	PN7 (hexanoyl-mimétique)	−5.0	Substrate analogue
	Platensimycine	−6.8	Standard inhibitor
FabG	STG	−8.8	Strigolactones
	5-DS	−8.7	
	STGA	−8.7	
	OROB	−8.7	
	TZROG	−8.6	Cytokinins
	NADPH	−9.3	Natural cofactor
	Luteolin	−8.3	Standard inhibitor

Table 2: *Cont.*

Target	Ligands	Binding Energies (kcal/mol)	Classes
FATA	OROB	−11.3	Strigolactones
	SGL	−11.0	
	5-DS	−10.7	
	GR24	−10.3	
	STG	−10.3	
	Oleic acid	−6.6	Substrate analogue
	WP2 (spirolactame)	−10.4	Standard inhibitor
GPAT	DHZMP	−8.8	Cytokinins
	CZ9G	−8.7	
	OROB	−8.6	Strigolactones
	IP9G	−8.5	Cytokinins
	TZROG	−8.5	
	Sn-glycerol-3-phosphate	−4.7	Natural substrate
	FSG67	−5.9	Standard inhibitor

3.3 Ligand Receptor Interactions

The specific interactions between the selected ligands and microalgal enzymes were analyzed, with binding residues summarized in Table S4 (Supplementary Data). For FabD, the strigolactones, (+)-strigyl acetate (STGA) was predicted to to form three hydrogen bonds (ASN152, GLN156, and LYS182) and two alkyl contacts (LEU181 and LYS182) within the active site (Fig. 1A). These residues are located near conserved positions (ARG, SER, HIS, GLN, and LEU) that contribute to FabD catalytic function [14,36]. The predicted STGA binding mode partially overlaps with that of the natural substrate malonyl-CoA, which engages residues such as GLN10, GLN13, HIS87×2, ASN150, GLN156, SER12, GLY11, and SER88, and also shares contacts with the standard inhibitor corytuberine. Such overlapping interactions suggest possible competition with malonyl-CoA or reference inhibitors at the initiation site of FAS II, pending experimental validation.

In the predicted complex between cis-zeatin-O-glucoside (ZOG) and β-ketoacyl-acyl carrier protein synthase II (KASII), the ligand was predicted to form eight hydrogen bonds: five conventional interactions (ILE273, ASN407, ASN314, and ALA209×2) and three carbon-hydrogen contacts (THR274, PHE401, and ARG210) (Fig. 1B). These residues are situated in the immediate vicinity of the key catalytic quadruplet (CYS172, HIS307, LYS339, and HIS344). PHE401 has been described as a “gatekeeper” residue that undergoes conformational changes to regulate access to the binding pocket. The active site crevice, defined by a network of residues, including ASP269, THR274, PRO276, GLY280, ALA283, THR309, THR311, ALA313, ASN314, THR317, GLU318, GLY402, PHE403, GLY405, HIS406, and ASN407 [15], provides a candidate environment for ZOG interactions. Compared to with the substrate analogue PN7 and the inhibitor platensimycin, which engage catalytic and elongation residues more directly, ZOG appears to interact less directly with the elongation site. This binding pattern is consistent with a candidate interaction near residues involved in the first elongation step of type II fatty acid synthesis [37]. Experimental validation will be required to determine whether such interactions translate into activation, inhibition, or allosteric modulation.

In the predicted complex between 3-oxoacyl ACP reductase (FabG) and (+)-strigol (STG), hydrogen bonds were observed with ARG18, TYR158, LYS162, and GLY95, together with hydrophobic interactions involving ALA40 and ALA94 (Fig. 1C). These residues are located near the conserved catalytic triad (SER, TYR, LYS) and an asparagine residue that contribute to FabG activity [36,38,39]. The predicted STG binding profile partially overlaps with that of the cofactor NADPH and the standard inhibitor luteolin, which also

engage residues at the cofactor-binding region. This overlap suggests a candidate interaction consistent with possible competition at the NADPH-binding site. Whether such binding events result in activation, inhibition, or allosteric modulation remains to be determined through enzymatic validation.

In the predicted complex between (+)-orobanchol (OROB) and acyl-ACP thioesterase (FATA), an α/β hydrolase involved in terminating fatty acid elongation, three hydrogen bonds were observed (ALA137, ARG182×2) together with hydrophobic contacts involving ALA121 and TRP202 (Fig. 1D). These predicted interactions resemble those reported for the substrate analogue oleic acid and the inhibitor WP2, which also engage residues such as TRP202, ALA121/125/137, PHE147, and ARG182. The overlap in hydrophobic contacts suggests that OROB may share candidate binding features with both substrate and inhibitor at the C16–C18 chain-termination site. This observation is consistent with the quantitative model proposed by Jing et al. [40], who identified 22 amino acid residues mainly located within the N-terminal hot-dog fold of the predicted CvFatB2a structure, including ARG124, ARG125, ALA63, and ALA192, which are likely involved in substrate specificity through modulation of enzyme–ACP interactions. Further experimental studies will be required to clarify whether such binding corresponds to functional modulation of FATA activity.

Finally, glycerol-3-phosphate acyltransferase (GPAT), which catalyzes the first rate-limiting step of *de novo* glycerolipid synthesis [41], was predicted to interact with DHZMP. The binding profile included an electrostatic interaction with ASP253, ten hydrogen bonds (SER193, LYS194, VAL191, GLU144, GLY235×3, ALA232, GLY170, and HIS141), and five hydrophobic interactions (ALA169, PRO147, VAL173, LEU188, and TYR167) (Fig. 1E). These predicted contacts overlap with catalytically relevant regions of GPAT, involving ASP253, LYS194, and GLU144. Previous studies [18] reported similar binding sites in MiGPAT1, where ACP interacts via hydrogen bonds and electrostatic forces to stabilize the acyl intermediate. The observed DHZMP binding pattern also partially resembles that of sn-glycerol-3-phosphate and the inhibitor FSG67, consistent with a candidate interaction at the sn-1 acylation site. Additional *in vitro* assays will be needed to evaluate if the predicted binding translates into functional modulation of GPAT activity.

3.4 Molecular Dynamics

Molecular dynamic (MD) simulations were performed to explore the conformational stability and dynamic behavior of the protein–ligand complexes [42]. Stability was assessed using RMSD, RMSF, hydrogen bond profiles, radius of gyration (Rg), and solvent-accessible surface area (SASA). RMSD provides an overview of conformational stability, RMSF highlights residue-level flexibility, hydrogen bonds contribute to binding persistence, Rg reflects structural compactness, and SASA indicates solvent exposure [43]. For the STGA/FabD complex (Fig. 2), the backbone RMSD remained within ~0.1 nm, whereas the complex RMSD stabilized between 0.5–0.7 nm. The ligand RMSD was below 0.2 nm, and RMSF values were generally <0.3 nm. Stable Rg (1.37–1.67 nm) and SASA (125–140 nm^2), together with 1–3 persistent hydrogen bonds, are consistent with a compact structure and limited conformational rearrangement.

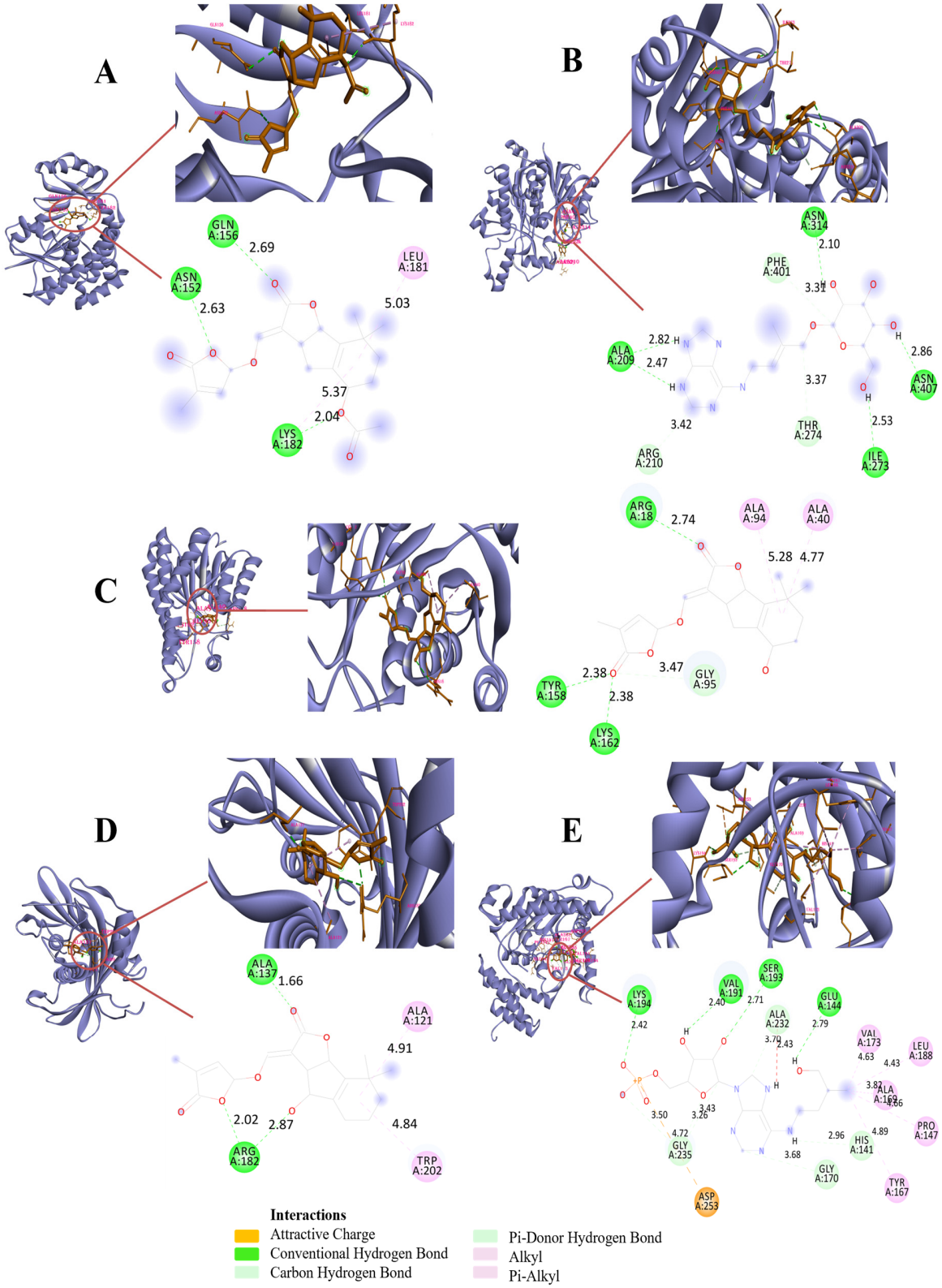

Figure 1: Molecular docking of STGA/FabD (**A**), ZOG/KASII (**B**), STG/FabG (**C**), OROB/FATA (**D**), and DHZMP/GPAT (**E**) complexes and the interaction residues.

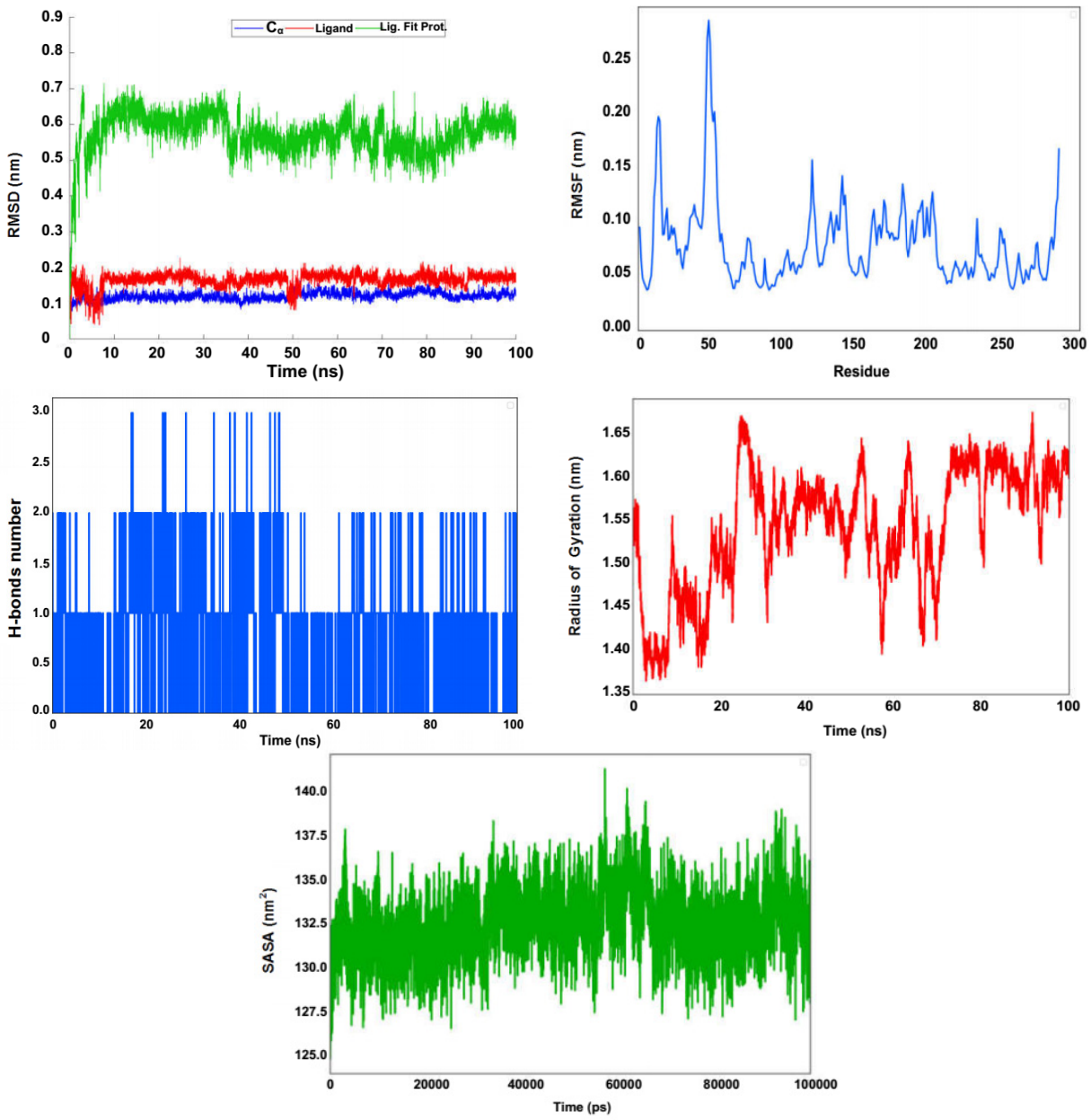

Figure 2: MD simulation of STGA/FabD complex during 100 ns (RMSD, RMSF, H-bonds, Rg, and SASA profiles).

In the ZOG/KASII complex (Fig. 3), the backbone RMSD stabilized between 0.1–0.25 nm, with ligand RMSD <0.3 nm. The complex RMSD plateaued at 0.6–0.88 nm (20–70 ns) before converging to 0.4–0.6 nm. RMSF values were <0.3 nm, with localized flexibility in residues 100–150. Stable SASA (156–174 nm^2), Rg (1.55–1.85 nm), and 1–11 hydrogen bonds suggest a well-maintained binding mode.

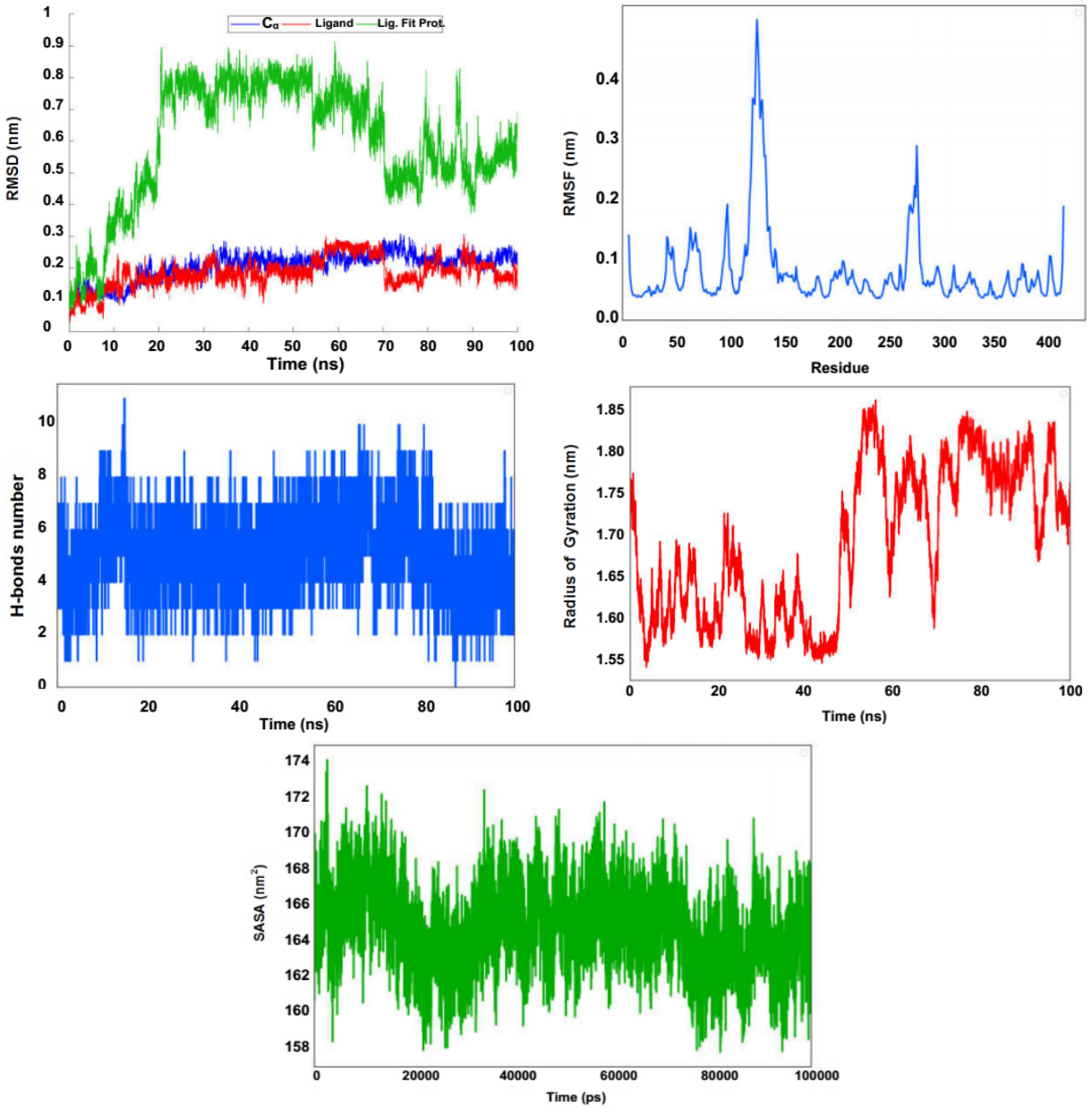

Figure 3: MD simulation of ZOG/KASII complex during 100 ns (RMSD, RMSF, H-bond, Rg, and SASA profiles).

For the STG/FabG system (Fig. 4), backbone RMSD remained within 0.1–0.3 nm, while ligand RMSD was <0.2 nm. A gradual increase in complex RMSD toward the end of the simulation suggested ligand repositioning. RMSF highlighted flexibility in loop regions (100–110 and 200–220). Variations in Rg (1.25–1.60 nm) and SASA (111–127 nm^2) are consistent with partial ligand displacement, although 1–5 hydrogen bonds were maintained.

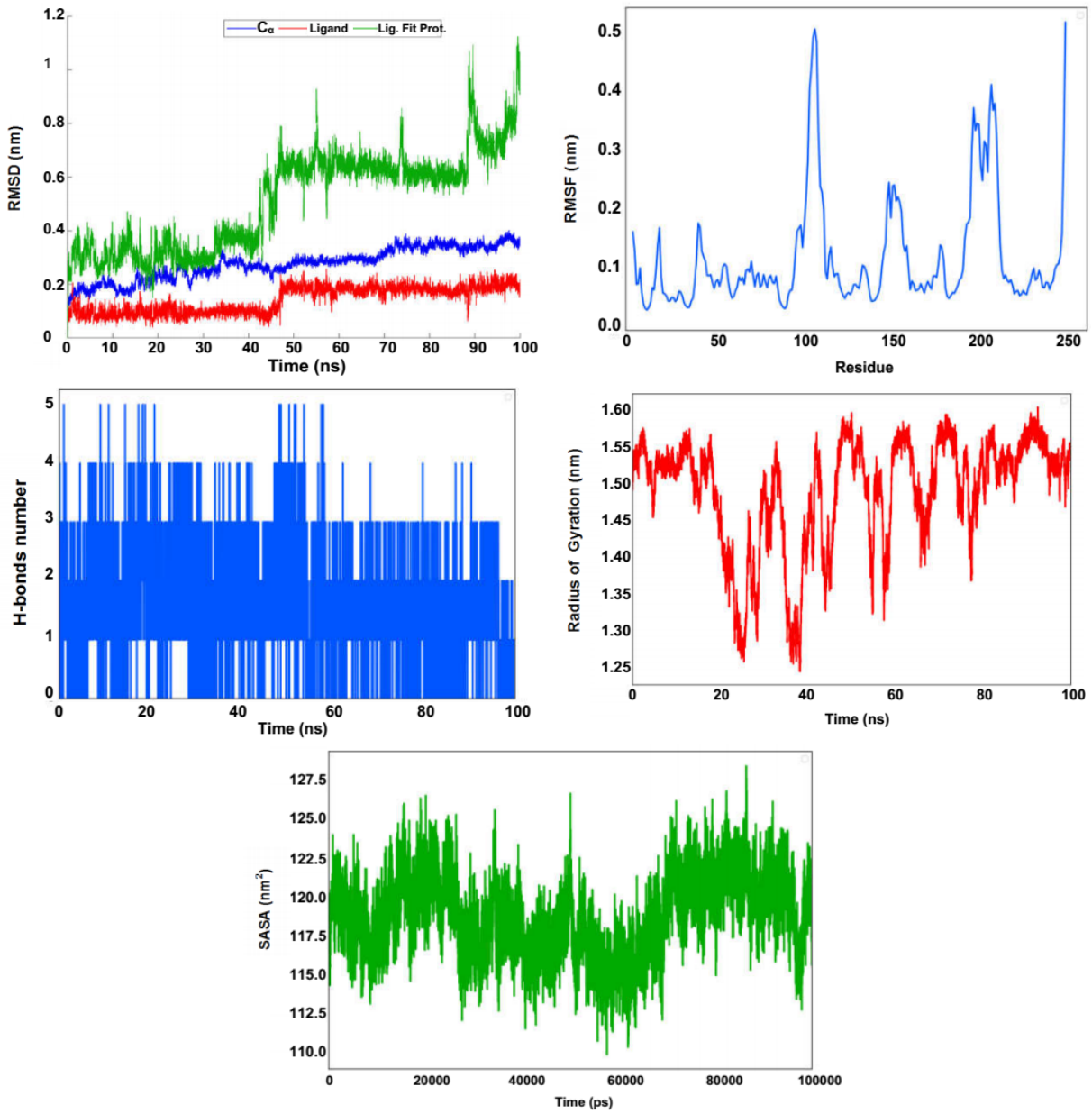

Figure 4: MD simulation of STG/FabG complex during 100 ns (RMSD, RMSF, H-bonds, Rg, and SASA profiles).

The OROB/FATA complex (Fig. 5) reached equilibrium rapidly, with protein and ligand RMSD stabilizing below 0.4 nm after 10 ns. RMSF analysis revealed expected flexibility in terminal and loop regions. Stable hydrogen bonding (1–4 interactions), SASA (~145–163 nm^2), and Rg (1.4–1.8 nm) support a compact and equilibrated structure.

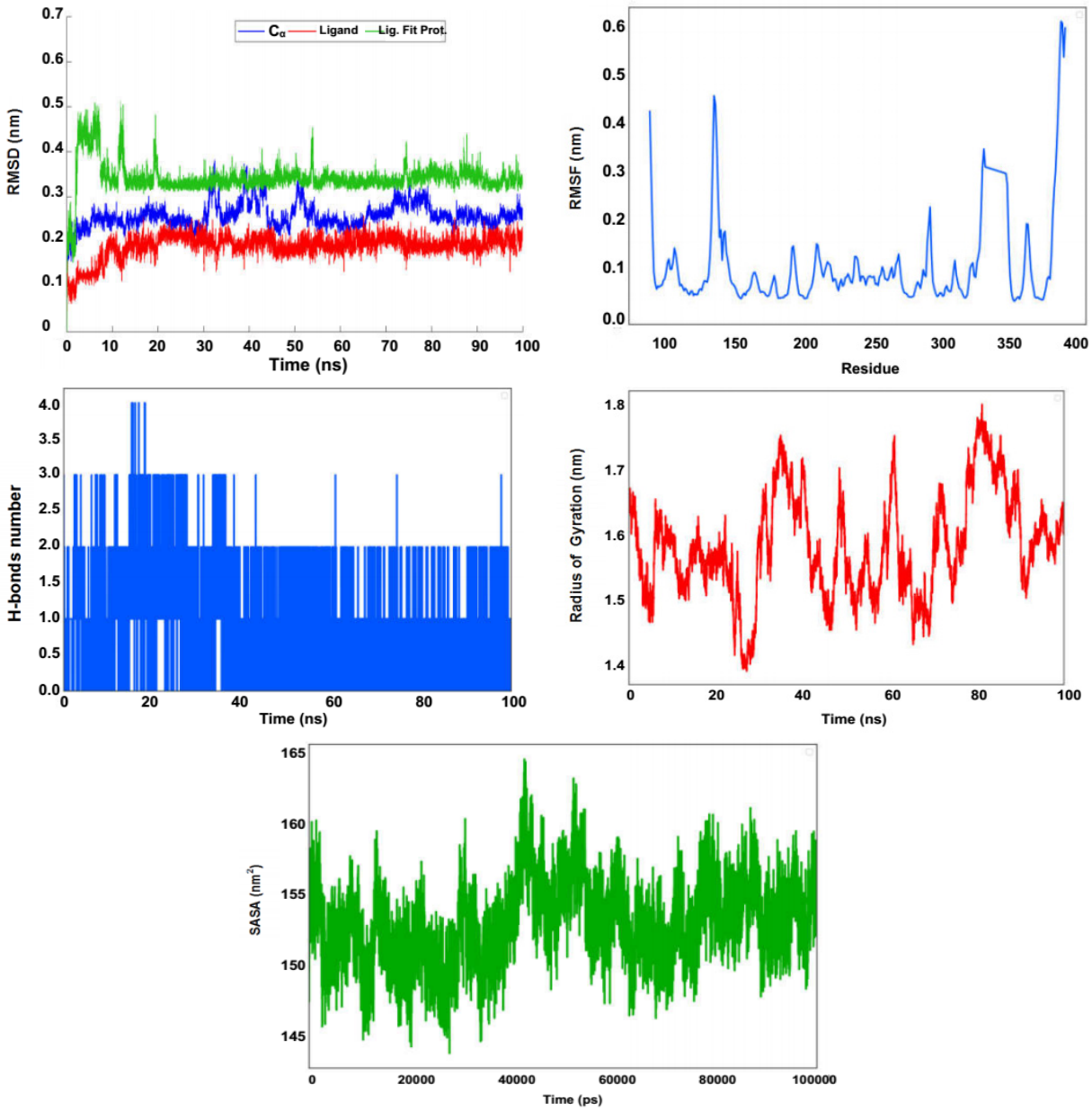

Figure 5: MD simulation of OROB/FATA complex during 100 ns (RMSD, RMSF, H-bonds, Rg, and SASA profiles).

Similarly, the DHZMP/GPAT complex (Fig. 6) exhibited stable dynamics, with RMSD values maintained between 0.15–0.2 nm over 100 ns. Ligand and protein RMSD stabilized at ~0.15 and ~0.3 nm, respectively. RMSF indicated limited flexibility confined to the N-terminal region, whereas active site residues remained stable. Persistent hydrogen bonding (1–10 interactions), along with stable Rg (1.5–2.0 nm) and SASA (172–190 nm^2), confirmed structural integrity.

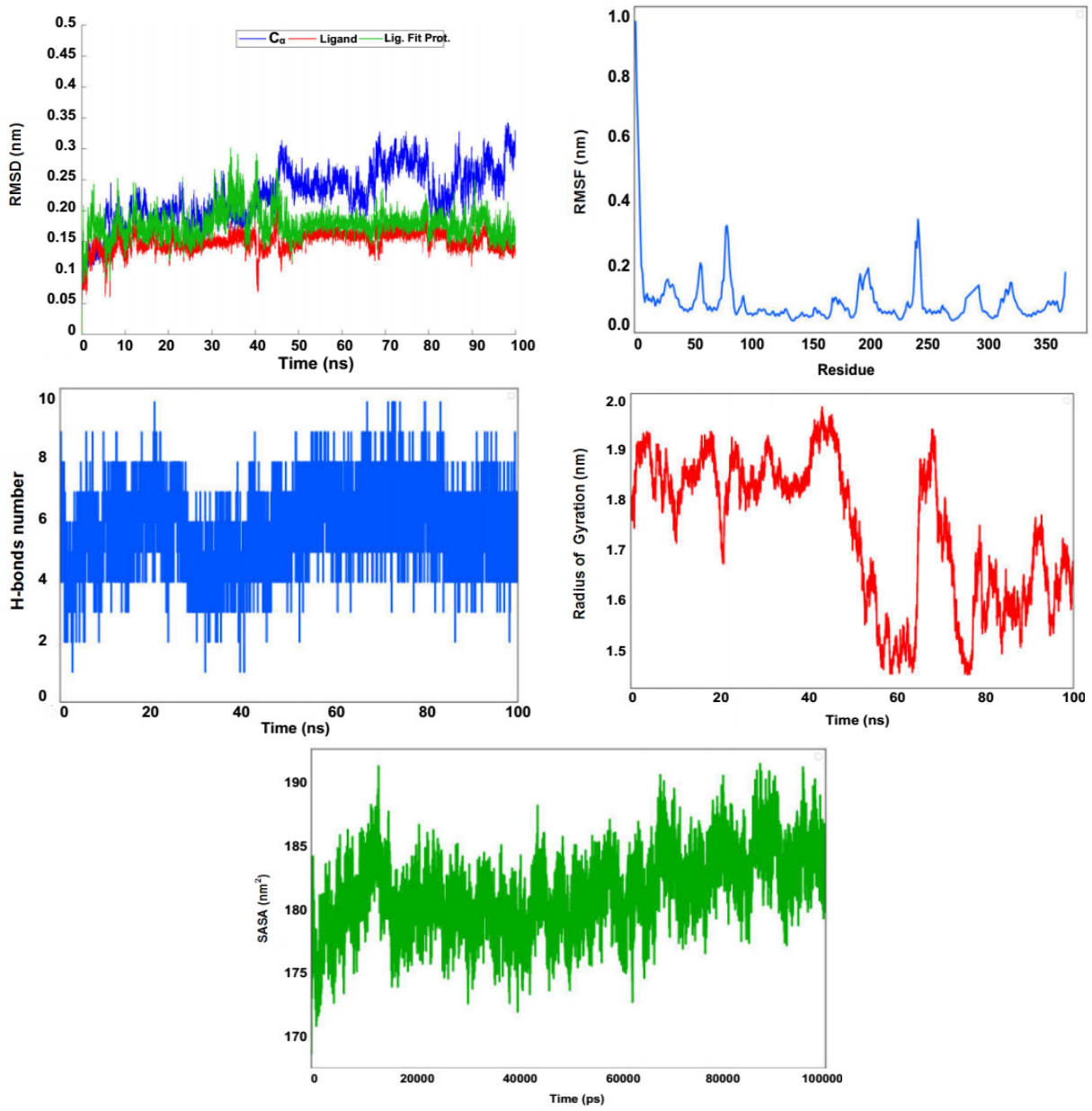

Figure 6: MD simulation of DHZMP/GPAT complex during 100 ns (RMSD, RMSF, H-bonds, Rg, and SASA profiles).

Overall, all complexes maintained stable binding modes with limited backbone deviations and persistent key interactions throughout the simulations. These findings support the structural plausibility of the docking poses; however, they reflect only conformational stability, and the potential effects on catalytic efficiency or pathway flux must be validated through enzymatic and cellular experiments.

3.5 Density Functional Theory

3.5.1 Frontier Molecular Orbital (FMO) Analysis

Frontier molecular orbital (FMO) analysis was performed to characterize the electronic properties of the candidate ligands. Total energy values (−1113.31 to −1806.39 Hartrees) reflect intrinsic electronic stability, with more negative values indicating greater stability. Dipole moments ranged from 4.08 to 9.07 Debye,

suggesting variable polarity that may influence potential interactions. Higher HOMO energies are associated with enhanced electron-donating capacity, whereas lower LUMO energies indicate increased electrophilicity, polarization, and intramolecular charge transfer, which may contribute to candidate binding potential [43]. The HOMO–LUMO energy gap (2.96–5.22 eV) provides an index of reactivity and stability. Fig. 7 shows the atomic orbital components of these compounds. For example, ZOG exhibited a relatively large gap (5.22 eV), consistent with kinetic stability and a "hard" electronic character [44]. In contrast, DHZMP displayed a smaller gap (2.96 eV), consistent with a "soft" system that is more polarizable and reactive [45]. These descriptors provide a theoretical basis for prioritizing ligands as supplementary electronic characterizations, highlighting their ability to adapt electron density to enzyme active-site environments and potentially favor interactions with polar residues or intermediates. Their biological relevance remains qualitative and requires experimental validation.

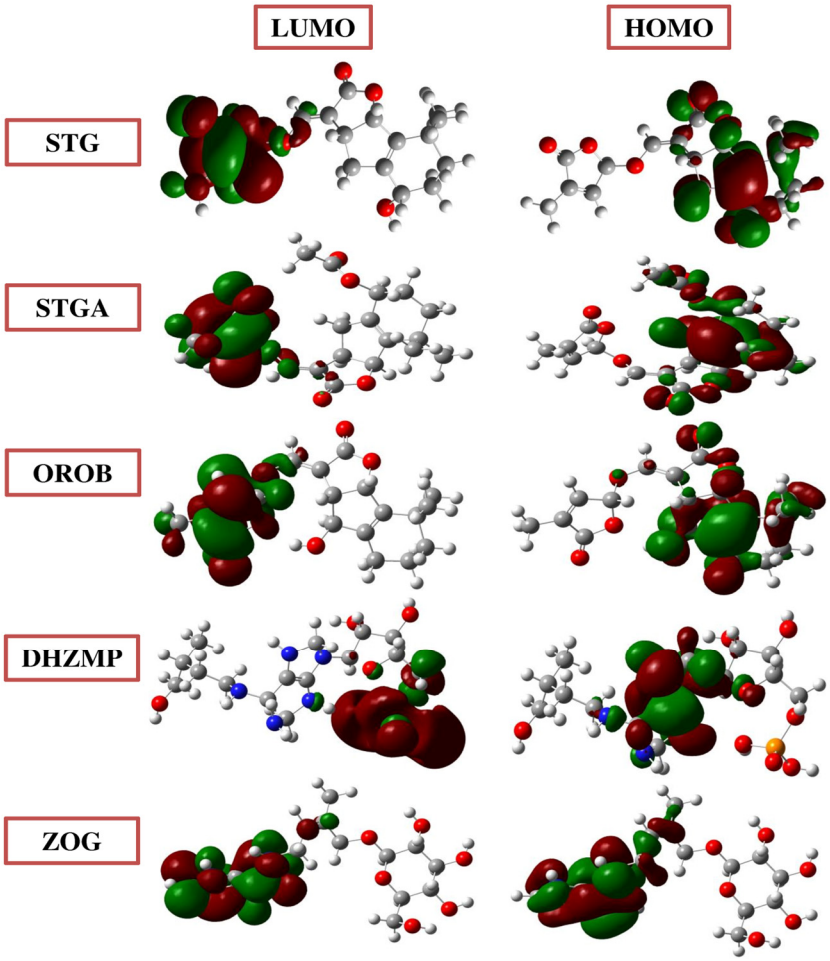

Figure 7: Molecular boundary orbitals of STG, STGA, OROB, DHZMP, and ZOG.

3.5.2 Global Chemical Reactivity Descriptors (GCRD)

HOMO and LUMO energies are related to ionization potentials and electron affinities. The ionization energies (4.38–6.84 eV) indicate thermal stability, while the electron affinities (1.14–2.65 eV) suggest moderate electron-accepting capacity. Absolute hardness values (1.48–2.61 eV) reflect resistance to electron exchange, whereas global softness (0.19–0.33 eV^{-1}) highlights the ease with which electrons can be redistributed under

external perturbation [44]. The negative chemical potential (−2.90 to −4.73 eV) is consistent with electronic stability, while electronegativity values (2.90–4.73 eV) reflect the tendency to capture electrons for bond formation. Notably, strigolactones (STG, STGA, OROB) exhibited relatively high electrophilicity indices, suggesting a stronger tendency to accept electron density. This observation is consistent with candidate interactions at catalytically relevant regions, particularly nucleophilic residues [43] (Table 3). Experimental studies will be required to clarify whether such electronic properties correspond to functional modulation of enzyme activity.

Table 3: Global chemical reactivity descriptors of the five PGR compounds.

Compound	Total Energy	HOMO Energy	LUMO Energy	ΔE	Dipole Moment	η	μ	ω	σ	χ	IE	EA
STG	−1188.52	−6.81	−2.29	4.52	9.07	2.26	−4.55	4.58	0.22	4.55	6.81	2.29
STGA	−1341.17	−6.84	−2.59	4.25	4.08	2.12	−4.71	5.23	0.23	4.71	6.84	2.59
OROB	−1188.52	−6.82	−2.65	4.17	6.06	2.08	−4.73	5.37	0.24	4.73	6.82	2.65
DHZMP	−1806.39	−4.38	−1.42	2.96	5.74	1.48	−2.90	2.84	0.33	2.90	4.38	1.42
ZOG	−1348.51	−6.36	−1.14	5.22	7.38	2.61	−3.75	2.69	0.19	3.75	6.36	1.14

Note: Total energy (Hartrees), dipole moment (Debye), and other parameters (eV).

3.5.3 Molecular Electrostatic Potential (MEP)

Molecular electrostatic potential (MEP) maps (Fig. 8) were generated to visualize electrophilic and nucleophilic regions predicted to participate in non-covalent interactions [27]. In strigolactones, negative potentials regions (red) localized on oxygen atoms of the cyclohexene and γ-butyrolactone rings suggest candidate hydrogen bonding or electrostatic contacts. For DHZMP, negative regions around the N–H groups of the purine ring (bicyclic A–B) and the O–P group of the side chain are consistent with predicted hydrogen bonding and electrostatic interactions with GPAT. These spatial distributions qualitatively support the interaction patterns observed in docking and MD simulations.

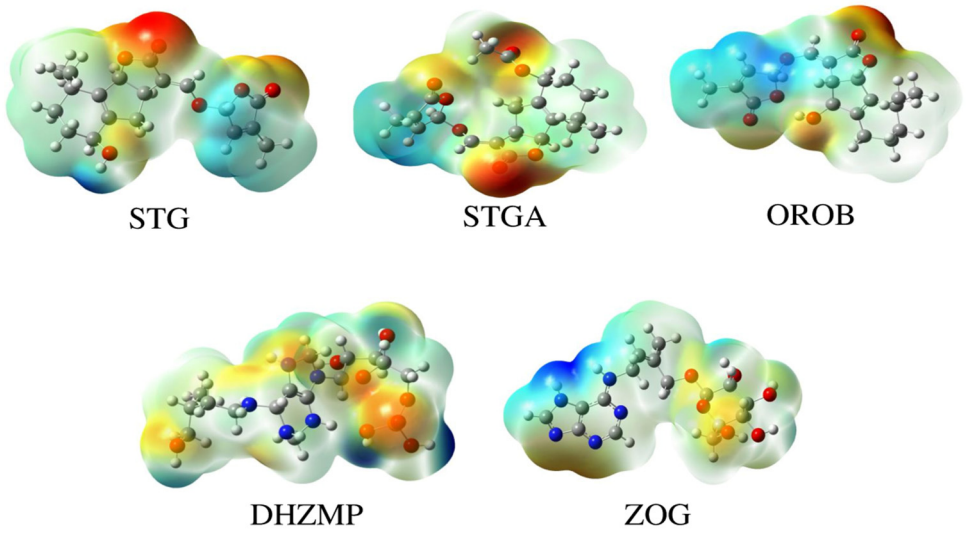

Figure 8: Molecular electrostatic potentials of STG, STGA, OROB, DHZMP, and ZOG.

DFT-derived descriptors provide useful insights into the intrinsic electronic properties of ligands under gas-phase conditions and do not capture the full complexity of the biological environment. Therefore, these

results should be interpreted as supplementary, rather than predictive of catalytic activity. Any mechanistic conclusions will require advanced modeling approaches, such as QM/MM calculations, together with experimental validation.

4 Conclusion

This *in silico* study represents an exhaustive screening of sixty-five plant growth regulators against key microalgal enzymes (FabD, KASII, FabG, FATA, and GPAT) involved in lipid metabolism. Through a multi-layered computational approach, strigolactones and cytokinins–specifically OROB, DHZMP, and STGA–were prioritized as candidate binders for further investigation. Their predicted binding energies, dynamic stability profiles, and complementary electronic descriptors provide a computational rationale for possible interactions at catalytically relevant regions of microalgal lipid metabolism. These hypothesis-generating results require experimental validation through enzymatic assays, microalgal cultivation, lipid quantification, and gene expression analyses to determine their biological relevance. Such efforts will be critical in guiding the rational design of biostimulation strategies aimed at optimizing microalgal lipid productivity and strengthening the economic viability of sustainable biofuels.

Acknowledgement: The authors would like to sincerely thank Prof. El Hadj Elandaloussi and Dr. Abdelwahed Benadda for their careful revision of the manuscript. Their insightful comments and dedicated support have significantly improved the quality and readiness of this work.

Funding Statement: The authors received no specific funding for this study.

Author Contributions: Conceptualization: Hanane Oucif; methodology: Hanane Oucif, Miloud Benaissa; formal analysis: Hanane Oucif, Leila Saddikioui; investigation and data analysis: Hanane Oucif, Zineb Belhamra; software: Hanane Oucif; resources: Djilali Baghdadi; validation: Hanane Oucif, Meriem F. Meliani; visualization: Nadia Y. Asfouri; writing—original draft preparation: Hanane Oucif; Miloud Benaissa; writing—review and editing: Hanane Oucif, Miloud Benaissa. All authors reviewed and approved the final version of the manuscript.

Availability of Data and Materials: All data collected or analyzed during this investigation are included in this paper.

Ethics Approval: Not applicable.

Conflicts of Interest: The authors declare no conflicts of interest.

Supplementary Materials: The supplementary material is available online at https://www.techscience.com/doi/10.32604/phyton.2026.080926/s1.

References

1. Ahmad A, Banat F, Alsafar H, Hasan SW. Recent breakthroughs in integrated biomolecular and biotechnological approaches for enhanced lipid and carotenoid production from microalgae. Phytochem Rev. 2023;22(4):993–1013. [CrossRef].
2. Narayanan I, Pandey S, Vinayagam R, Selvaraj R, Varadavenkatesan T. A recent update on enhancing lipid and carbohydrate accumulation for sustainable biofuel production in microalgal biomass. Discov Appl Sci. 2025;7(3):195. [CrossRef].
3. Wang M, Ye X, Bi H, Shen Z. Microalgae biofuels: Illuminating the path to a sustainable future amidst challenges and opportunities. Biotechnol Biofuels Bioprod. 2024;17(1):10. [CrossRef].
4. Xin Y, Wu S, Miao C, Xu T, Lu Y. Towards lipid from microalgae: Products, biosynthesis, and genetic engineering. Life. 2024;14(4):447. [CrossRef].

5. Behera B, Unpaprom Y, Ramaraj R, Maniam GP, Govindan N, Paramasivan B. Integrated biomolecular and bioprocess engineering strategies for enhancing the lipid yield from microalgae. Renew Sustain Energy Rev. 2021;148:111270. [CrossRef].
6. Song Y, Wang F, Chen L, Zhang W. Engineering fatty acid biosynthesis in microalgae: Recent progress and perspectives. Mar Drugs. 2024;22(5):216. [CrossRef].
7. Gasperini D, Howe GA. Phytohormones in a universe of regulatory metabolites: Lessons from jasmonate. Plant Physiol. 2024;195(1):135–54. [CrossRef].
8. Stirk WA, van Staden J. Potential of phytohormones as a strategy to improve microalgae productivity for biotechnological applications. Biotechnol Adv. 2020;44:107612. [CrossRef].
9. Parsaeimehr A, Mancera-Andrade EI, Robledo-Padilla F, Iqbal HMN, Parra-Saldivar R. A chemical approach to manipulate the algal growth, lipid content and high-value alpha-linolenic acid for biodiesel production. Algal Res. 2017;26:312–22. [CrossRef].
10. Żeruń J, Bajguz A. Around the brassinosteroids in algae. Algal Res. 2025;85:103881. [CrossRef].
11. Del Mondo A, Vinaccia A, Pistelli L, Brunet C, Sansone C. On the human health benefits of microalgal phytohormones: An explorative *in silico* analysis. Comput Struct Biotechnol J. 2023;21:1092–101. [CrossRef].
12. Kim S, Chen J, Cheng T, Gindulyte A, He J, He S, et al. PubChem 2025 update. Nucleic Acids Res. 2025;53(D1):D1516–25. [CrossRef].
13. Hanwell MD, Curtis DE, Lonie DC, Vandermeersch T, Zurek E, Hutchison GR. Avogadro: An advanced semantic chemical editor, visualization, and analysis platform. J Cheminform. 2012;4(1):17. [CrossRef].
14. Liu Y, Feng Y, Wang Y, Li X, Cao X, Xue S. Structural and biochemical characterization of MCAT from photosynthetic microorganism *Synechocystis* sp. PCC 6803 reveal its stepwise catalytic mechanism. Biochem Biophys Res Commun. 2015;457(3):398–403. [CrossRef].
15. Moche M, Dehesh K, Edwards P, Lindqvist Y. The crystal structure of β-ketoacyl-acyl carrier protein synthase II from *Synechocystis* sp. at 1.54 Å resolution and its relationship to other condensing enzymes 1 1 Edited by R. Huber. J Mol Biol. 2001;305(3):491–503. [CrossRef].
16. Chen C, Zhuang NN, Lee KH. 3-oxoacyl-[acyl-carrier-protein] reductase from Synechococcus elongatus PCC 7942 in complex with NADP: 4dmm [Internet]. [cited 2026 Jan 1]. Available from: https://www.rcsb.org/structure/4DMM.
17. Chen JA, Suo Y, Mayfield SP, Burkart MD. Structural characterization of an endogenous algal acyl-ACP thioesterase. Biochemistry. 2025;64(16):3508–14. [CrossRef].
18. Li X, Yang M, Sun D, Shi J, Yang M, Feng Y, et al. Unique recognition of the microalgal plastidial glycerol-3-phosphate acyltransferase for acyl-ACP. Plant Sci. 2023;332:111725. [CrossRef].
19. Dassault Systèmes BIOVIA. Discovery Studio Visualizer. San Diego, CA, USA: Dassault Systèmes; 2024.
20. Guex N, Peitsch MC. SWISS-MODEL and the Swiss-Pdb Viewer: An environment for comparative protein modeling. Electrophoresis. 1997;18(15):2714–23. [CrossRef].
21. Dallakyan S, Olson AJ. Small-molecule library screening by docking with PyRx. In: Chemical biology. New York, NY, USA: Springer; 2014. p. 243–50. [CrossRef].
22. Abraham M, Alekseenko A, Basov V, Bergh C, Briand E, Brown A, et al. GROMACS 2024.1 Source code. Zenodo; 2024 [cited 2026 Jan 1]. Available from: https://zenodo.org/records/10721181.
23. Holmboe M. Import and plot Gromacs .xvg data files. MATLAB Central File Exchange; [cited 2026 Jan 1]. Available from: https://www.mathworks.com/matlabcentral/fileexchange/70607-import-and-plot-gromacs-xvg-data-files.
24. Frisch MJ, Trucks GW, Schlegel HB, Scuseria GE, Robb MA, Cheeseman JR, et al. Gaussian 09, Revision D.01. Wallingford, CT, USA: Gaussian, Inc.; 2009.
25. Becke AD. Density-functional thermochemistry. III. The role of exact exchange. J Chem Phys. 1993;98(7):5648–52. [CrossRef].
26. Dennington R, Keith TA, Millam JM. GaussView version 5.0.8. Wallingford, CT, USA: Gaussian, Inc.; 2009.
27. Abu-Izneid T, Rauf A, Ahmad Z, Wadood A, Ayub K, Muhammad N, et al. Density functional theory (DFT), molecular docking, and xanthine oxidase inhibitory studies of dinaphthodiospyrol S from *Diospyros kaki* L. Saudi Pharm J. 2024;32(2):101936. [CrossRef].

28. Du H, Ahmed F, Lin B, Li Z, Huang Y, Sun G, et al. The effects of plant growth regulators on cell growth, protein, carotenoid, PUFAs and lipid production of *Chlorella pyrenoidosa* ZF strain. Energies. 2017;10(11):1696. [CrossRef].
29. Du H, Ren J, Li Z, Zhang H, Wang K, Lin B, et al. Plant growth regulators affect biomass, protein, carotenoid, and lipid production in *Botryococcus braunii*. Aquac Int. 2020;28(3):1319–40. [CrossRef].
30. Lin B, Ahmed F, Du H, Li Z, Yan Y, Huang Y, et al. Plant growth regulators promote lipid and carotenoid accumulation in *Chlorella vulgaris*. J Appl Phycol. 2018;30(3):1549–61. [CrossRef].
31. Correa-Aguado CH, Cerrillo-Rojas V, Rocha-Uribe A, Soria-Guerra E, Morales-Dominguez J. Benzyl Amino Purine and Gibberellic Acid Coupled to Nitrogen-Limited Stress Induce Fatty Acids, Biomass Accumulation, and Gene Expression in Scenedesmus Obliquus. Phyton. 2021;90:515–31. [CrossRef].
32. Sivaramakrishnan R, Incharoensakdi A. Plant hormone induced enrichment of *Chlorella* sp. omega-3 fatty acids. Biotechnol Biofuels. 2020;13(1):7. [CrossRef].
33. Han X, Zeng H, Bartocci P, Fantozzi F, Yan Y. Phytohormones and effects on growth and metabolites of microalgae: A review. Fermentation. 2018;4(2):25. [CrossRef].
34. Song X, Zhao Y, Han B, Li T, Zhao P, Xu JW, et al. Strigolactone mediates jasmonic acid-induced lipid production in microalga *Monoraphidium* sp. QLY-1 under nitrogen deficiency conditions. Bioresour Technol. 2020;306:123107. [CrossRef].
35. Guldhe A, Renuka N, Singh P, Bux F. Effect of phytohormones from different classes on gene expression of *Chlorella* sorokiniana under nitrogen limitation for enhanced biomass and lipid production. Algal Res. 2019;40:101518. [CrossRef].
36. Bibens L, Becker JP, Dassonville-Klimpt A, Sonnet P. A review of fatty acid biosynthesis enzyme inhibitors as promising antimicrobial drugs. Pharmaceuticals. 2023;16(3):425. [CrossRef].
37. He M, Qin CX, Wang X, Ding NZ. Plant unsaturated fatty acids: Biosynthesis and regulation. Front Plant Sci. 2020;11:390. [CrossRef].
38. Hu Z, Ma J, Chen Y, Tong W, Zhu L, Wang H, et al. Escherichia coli FabG 3-ketoacyl-ACP reductase proteins lacking the assigned catalytic triad residues are active enzymes. J Biol Chem. 2021;296:100365. [CrossRef].
39. Zhou J, Zhang L, Wang Y, Song W, Huang Y, Mu Y, et al. The molecular basis of catalysis by SDR family members ketoacyl-ACP reductase FabG and enoyl-ACP reductase FabI in type-II fatty acid biosynthesis. Angew Chem Int Ed. 2023;62(46):e202313109. [CrossRef].
40. Jing F, Chen K, Yandeau-Nelson MD, Nikolau BJ. Machine learning model of the catalytic efficiency and substrate specificity of acyl-ACP thioesterase variants generated from natural and *in vitro* directed evolution. Front Bioeng Biotechnol. 2024;12:1379121. [CrossRef].
41. Yu J, Loh K, Song ZY, Yang HQ, Zhang Y, Lin S. Update on glycerol-3-phosphate acyltransferases: The roles in the development of insulin resistance. Nutr Diabetes. 2018;8(1):34. [CrossRef].
42. Boakye A, Seidu MP, Adomako A, Laryea MK, Borquaye LS. Marine-derived furanones targeting quorum-sensing receptors in *Pseudomonas aeruginosa*: Molecular insights and potential mechanisms of inhibition. Bioinform Biol Insights. 2024;18:11779322241275843. [CrossRef].
43. Sadeghian Z, Bayat M, Gheidari D. Synthesis, molecular docking, pharmacological evaluation, MD simulation, and DFT calculations of quinazolin-12-one derivatives as PDK1 inhibitors. Nanoscale Adv. 2025;7(18):5760–83. [CrossRef].
44. Choudhary V, Bhatt A, Dash D, Sharma N. DFT calculations on molecular structures, *HOMO*-LUMO study, reactivity descriptors and spectral analyses of newly synthesized diorganotin(IV) 2-chloridophenylacetohydroxamate complexes. J Comput Chem. 2019;40(27):2354–63. [CrossRef].
45. Farrokhnia M. Density functional theory studies on the antioxidant mechanism and electronic properties of some bioactive marine meroterpenoids: Sargahydroquionic acid and sargachromanol. ACS Omega. 2020;5(32):20382–90. [CrossRef].